Journal of
Synchrotron Radiation

ISSN 0909-0495

Received 1 November 2011
Accepted 18 May 2012

Interference phenomena of synchrotron radiation in TEY spectra for silicon-on-insulator structure

M. A. Andreeva,[a]* E. P. Domashevskaya,[b] E. E. Odintsova,[a] V. A. Terekhov[b] and S. Yu. Turishchev[b]

[a]Faculty of Physics, M. V. Lomonosov Moscow State University, Leninskie Gory, 119991 Moscow, Russian Federation, and [b]Voronezh State University, Universitetskaya pl. 1, 394006 Voronezh, Russian Federation. E-mail: mandreeva1@yandex.ru

The general matrix theory of the photoelectron/fluorescence excitation in anisotropic multilayer films at the total reflection condition of X-rays has been developed. In a particular case the theory has been applied to explain the oscillation structure of $L_{2,3}$ XANES spectra for a SiO_2/Si/SiO_2/c-Si sample in the pre-edge region which has been observed by a sample current technique at glancing angles of synchrotron radiation. Remarkably the phase of the oscillations is reversed by a $\sim 2^\circ$ angle variation. The observed spectral features are found to be a consequence of waveguide mode creation in the middle layer of strained Si, which changes the radiation field amplitude in the top SiO_2 layer. The fit of the data required the correction of the optical constants for Si and SiO_2 near the Si $L_{2,3}$-edges.

Keywords: XANES; total electron yield; X-ray standing waves; X-ray reflectivity.

1. Introduction

Total electron yield (TEY) or quantum yield (Y) (the latter is proportional to the compensatory photocurrent in TEY measurements) are well established methods for measuring spectra of X-ray absorption near-edge structure (XANES). Usually TEY spectra give a spectral shape similar to that of absorption spectra. The advantage of TEY or Y spectrum measurements is that they do not require the special thin-sample preparations that are needed for the direct absorption measurements. The effective sampling depth of the TEY technique, especially in the case of soft X-rays, is rather small ($\sim$2–5 nm) and is the reason for the excellent surface sensitivity of the method.

However, in recent years experimental evidence has been presented showing that in some cases an unexpected distortion of the TEY spectrum shape appears at X-ray glancing incidence angles and even at normal incidence (Ejima *et al.*, 1999; Terekhov *et al.*, 2010, 2011; Domashevskaya *et al.*, 2011). These results stimulated further investigations of TEY spectra at different glancing angles in order to find an explanation for the observed effects. For some samples extremely impressive modifications of the spectrum shape were obtained that show up as a periodic variation with the angle change (Domashevskaya *et al.*, 2011).

It is well known that for small glancing angles TEY is influenced by reflection from the surface. In the 1960s a simple formula was published (Rumsh *et al.*, 1961) that represented the number of created electrons dn in the differential layer dz,

$$\mathrm{d}n = (I_0/E)[1 - R(\theta)]\exp[-(\mu/\sin\theta)z](\mu/\sin\theta)\,\mathrm{d}z, \quad (1)$$

where $I_0 = N_0 hc/\lambda$ is the intensity of the incident radiation, E is the energy expenditure for the creation of one electron, λ is the incident photon wavelength, R is the reflectivity, θ is the glancing angle for the X-ray beam and μ is the linear absorption coefficient. In particular, from (1) it follows that if $R(\theta)$ is sufficiently small the TEY or Y from the surface is proportional to the absorption spectrum $\mu(\lambda)$. The similarity between the absorption and TEY spectra was demonstrated for the first time by Gudat & Kunz (1972).

The angular dependencies of TEY or fluorescence yield near the total external reflection angle have been well studied for soft and hard X-rays since the famous paper of Henke (1972), who presented a more accurate formula for dn,

$$\begin{aligned}\mathrm{d}n(\theta, z) &= S[1 - R(\theta)]\frac{\sin\theta}{\sin\theta'}\exp(-\mu z/\sin\theta')\rho\tau T(z)\,\mathrm{d}z,\\ T(z) &= \left[\exp(-\varepsilon_e z/\sin\psi)\right]/\sin\psi,\end{aligned} \quad (2)$$

where $S = I_0 A_0(\omega/4\pi)$ is the instrument constant, A_0 is the illuminated area, θ' is the glancing angle for the refracted wave, ρ is the volume density of the atoms, τ is the atomic cross section for the creation of the photoelectron, $T(z)$ is the function of the electron yield at depth z, ε_e is the linear electron-attenuation coefficient, and ψ is the glancing angle for the electron emission. In the simplest case, $\mu = \rho\tau$; however, in (2) ρ and τ can refer to specific q-type photoelectrons τ_q and density of atoms which can emit such photoelectrons ρ_q. Later a similar theory was developed by Solomin & Kruglov (1984).

Note that in the case of the reflection from a semi-infinite mirror the following exact relation takes place,

$$[1 - R(\theta)]\frac{\sin\theta}{\sin\theta'} = \left|1 + r(\theta)\right|^2, \quad (3)$$

where $r(\theta)$ is the Fresnel amplitude of reflectivity,

$$r = (\sin\theta - \eta)/(\sin\theta + \eta), \quad (4)$$

$$\eta = \left(\sin^2\theta + \chi\right)^{1/2}. \quad (5)$$

η is the normal component of the wavevector of the refracted wave in units of ω/c, $\sin\theta' = \mathrm{Re}(\eta)$, $\chi = (\varepsilon - 1)$ is the susceptibility of the reflecting medium, ε is its dielectric function. So TEY from the surface of a semi-infinite medium is initiated by the square module of the full electric field $|1 + r(\theta)|^2$, which was later called the standing wave at the surface (Bedzyk *et al.*, 1989).

A more general theory of TEY at the diffraction conditions from crystals has been developed (Afanas'ev & Kohn, 1978; Koval'chuk & Kohn, 1986). It was shown that the TEY angular dependency in the vicinity of the Bragg angle reflects the detailed structure of the radiation field inside the crystal (X-ray standing waves). It was demonstrated how it can be used for depth-selective analysis of imperfections of the crystal structure. Later (Bedzyk *et al.*, 1989; de Boer, 1991; Dev *et al.*, 2000), the standing-wave influence created at the total reflection conditions on the fluorescence or photoelectron yield was analysed as a function of the incidence angle. However, the problem of the proper determination of the function of the electron yield $T(z)$ (see, for example, Liljequist *et al.*, 1978; Kovalchuk *et al.*, 1986) imposes some limitations on the wide application of the TEY method. The fluorescence yield measurements have shown more advantages in the X-ray standing-wave method mostly due to its element sensitivity and also due to a much simpler form of the yield function $T(z)$ [see reviews by Vartanyants & Koval'chuk (2001) and von Bohlen (2009), and also recent papers (Lee *et al.*, 2006; Bera *et al.*, 2007; Gupta *et al.*, 2007; Novikova *et al.*, 2009; Andreeva *et al.*, 2009)].

The interpretation of the spectral dependencies of TEY from multilayers at glancing angles, where the reflectivity could not be ignored, has attracted minor attention up to the present. Reflectivity spectra near absorption edges in the soft X-ray region have been investigated in just a few works (Barchewitz *et al.*, 1978; Bremer *et al.*, 1980; Kaihola & Bremer, 1981; Jones & Woodruff, 1982; Andrė *et al.*, 1984; Lyakhovskaya *et al.*, 1988; van Brug *et al.*, 1989; Waki & Hirai, 1989; Filatova *et al.*, 1995, 1999, 2006). However, experiments at synchrotrons have presented ample opportunities for such measurements. Later, the magnetic effects at absorption edges, revealing themselves in the asymmetry of the reflectivity spectrum for different X-ray polarizations, attracted more attention (see, for example, Kao *et al.*, 1994; Knabben *et al.*, 1998; Sacchi, 1999; Goering *et al.*, 2001; Kim & Kortright, 2001; Oppeneer *et al.*, 2003; Andreeva *et al.*, 2006; Bergmann *et al.*, 2006). To our knowledge just one theoretical paper devoted to the TEY spectra at the total reflection conditions from multilayers has been published (Ejima, 2003). Later, this theory was applied to the interpretation of the experimental data (Watanabe *et al.*, 2006). Following the theory developed earlier for the case of thin films (Pepper, 1970), the waves in direct and opposite directions in each sublayer, as well as the influence of the interference of these waves on TEY, were taken into account. The formalism for the standing-wave description by Ejima (2003) was similar to that used by de Boer (1991) and Dev *et al.* (2000) devoted to the fluorescence emission. Note that the possibility to study the magnetic effects near the absorption edges requires the more general development of the standing-wave formalism for the case of anisotropic (magnetic) interactions of X-rays with multilayers at total reflection conditions.

A similar problem was considered earlier for Mössbauer radiation. Effects of the spectrum shape distortions for the conversion electron yield at grazing angles have been reported in several papers (Andreeva *et al.*, 1991, 1994, 1996, 1999). In these works the general theory of reflectivity from anisotropic multilayers was adjusted for consideration of the conversion electron Mössbauer spectra. This approximation could be easily used in the soft X-ray region as well. Use of the propagation matrices operating with the full field vectors simplifies the consideration of the standing-wave influence on the photoelectron/fluorescence excitation in an isotropic case and in addition allows the theory to be generalized to the case of anisotropic multilayers. The main difference in the matrix theory from the earlier theories (Ejima, 2003; de Boer, 1991; Dev *et al.*, 2000) (applicable only to the case of isotropic multilayers) is the rejection of consideration of waves in direct and opposite directions in each sublayer as well as their interference (a very cumbersome procedure especially in the anisotropic cases), and the performance of all computations with total field vectors.

Here we present the general 4×4-matrix theory of the standing-wave formation in anisotropic multilayers and their action on fluorescent quanta or photoelectron creation. We show as well how the propagation matrices are simplified in a particular case of isotropic interaction of X-rays with atoms. Then we apply our matrix algorithm for the interpretation of the quantum yield spectra measured from a SiO_2/Si/SiO_2 multilayer for the photon energy in the vicinity of the $L_{2,3}$ Si absorption edges at different glancing angles and find an explanation of the peculiarities of these spectra recently detected (Domashevskaya *et al.*, 2011).

2. Theory

We calculate the total photoelectron yield $Y(\omega)$ using the general formula

$$Y(\omega, \theta) = \int_0^\infty T(z)A(z, \omega, \theta)\,\mathrm{d}z, \quad (6)$$

where $A(z, \omega, \theta)$ is the number of electrons created at depth z and $T(z)$ is the function of the electron yield from depth z. This is a common approach where the photoelectron/fluorescence yield is considered in three steps: (i) we calculate how many photoelectrons or fluorescence quanta are created at

depth z by the electromagnetic radiation absorption; (ii) how these electrons or quanta will reach the detector or will be registered (*e.g.* in the induced-current technique); and (iii) perform the integration over all depths. Our efforts are mainly directed at the first step, and we rely upon famous papers by Henke (1972), Kasrai *et al.* (1996) and Ejima (2003) for the description of $T(z)$.

For the determination of the number of photoelectrons or fluorescent quanta $A(z, \omega, \theta)$ created in a differential layer dz we use the general energy conservation law (Born & Wolf, 1968; Fedorov, 1976),

$$\operatorname{div} \mathbf{S} + \frac{\partial W}{\partial t} = -Q, \tag{7}$$

where $\mathbf{S} = (c/4\pi)\mathrm{Re}[\mathbf{E}^* \times \mathbf{H}]$ is the Pointing vector averaged over time (the $\times$ sign means the vector product), $W = (c/8\pi)(\mathbf{E}^* \hat{\varepsilon}' \mathbf{E} + |\mathbf{H}|^2)$ is the density of the electromagnetic energy, and

$$Q = (\mathbf{E}^* \hat{\sigma} \mathbf{E}) \tag{8}$$

is the energy loss in unit volume at unit time (the superscript * sign denotes a complex conjugate). In (7) for the separation of gyrotropic and absorption effects the dielectric tensor $\hat{\varepsilon}$ is separated into two parts,

$$\hat{\varepsilon}' = (\hat{\varepsilon} + \hat{\varepsilon}^{\times})/2, \qquad \hat{\sigma} = (\omega/4\pi i)(\hat{\varepsilon} - \hat{\varepsilon}^{\times}/2), \tag{9}$$

where $\hat{\sigma}$ is the conductivity tensor, which determines the absorption processes (mainly photoabsorption for soft X-rays). The superscript $\times$ sign designates the Hermitian conjugated matrix. In non-gyrotropic media the tensor $\hat{\sigma}$ is simply the imaginary part of $\hat{\varepsilon}$. In gyrotropic media the imaginary components of $\hat{\varepsilon}$ can be responsible for the polarization effects, so the extraction of the absorptive part from $\hat{\varepsilon}$ is more complicated as in (9).

For the soft X-ray region the energy loss Q mainly determines the photon absorption and consequently the number of electrons or fluorescent quanta created at depth z in (6),

$$A \;\propto\; \tau(\mathbf{E}^* \hat{\sigma} \mathbf{E}) \;\propto\; \tau\left(\mathbf{E}^* \frac{\hat{\chi} - \hat{\chi}^{\times}}{\lambda} \mathbf{E}\right), \tag{10}$$

where $\hat{\chi} = \hat{\varepsilon} - 1$ is the tensor of susceptibility. If the medium contains different kinds of atoms then in (10) we should use the part of $\hat{\sigma}$ and $\hat{\chi}$ which is determined by the volume density ρ_q of the required kind of atoms, *i.e.* $\hat{\sigma}_q$ and $\hat{\chi}_q$. In our case we deal with the limited energy interval of the incident photons (95–105 eV) and consider τ as a constant parameter determining the number of photoelectrons or fluorescent quanta for one absorbed photon (but keeping in mind that this number can be specific for different layers).

Vector $\mathbf{E}$ in (10) represents the *total* electric field of radiation. If we use (10) it is not necessary to consider separately the waves in the direct and opposite directions and their interference influence in each layer on photoelectron creation as done by Ejima (2003). The convolution of the conductivity tensor $\hat{\sigma}$ with the electric field vectors $\mathbf{E}$ and $\mathbf{E}^*$ takes into account the possible anisotropy of the absorption process, because not only is the absolute value of the Pointing vector at the atom position essential but also the ability of the atom to respond to a given polarization of the electric field. A similar problem of anisotropic media with multipole interactions was analysed by Vartanyants & Zegenhagen (1997).

To our knowledge the simple expression (10) is the most general expression for the photoelectron or fluorescent quantum creation which is valid for any anisotropic or gyrotropic media. The other approach based on the eigen states of the electromagnetic waves in anisotropic layered media should take into account the interaction of atoms with four eigen waves and their interference fluxes (4 + 6 terms in total) which makes the calculations very cumbersome. Note that the problem of the eigen wave calculations in anisotropic media is also rather complicated (see, for example, Odintsova & Andreeva, 2010).

If ε is a scalar function (or the polarization of the radiation electric field $\mathbf{E}$ is one of the eigen polarization of the reflectivity task) then $\hat{\chi} - \hat{\chi}^{\times} = 2\,\mathrm{Im}(\chi)$ can be taken out of the convolution procedure and we easily obtain ($\omega = 2\pi c/\lambda$)

$$\begin{aligned} A(z, \omega, \theta) \;&\propto\; \tau\left\{\mathrm{Im}[\chi_q(z, \lambda)]/\lambda\right\}\left|E(z, \lambda, \theta)\right|^2 \\ &\propto\; \tau\mu_q(z, \lambda)\left|E(z, \lambda, \theta)\right|^2. \end{aligned} \tag{11}$$

The relation (11) establishes that the number of photoelectrons or fluorescent quanta created at depth z is proportional to the square module of the total radiation field amplitude at that depth, $|E(z, \omega, \theta)|^2$ (to the standing wave). In (11) we have taken into account that the imaginary part of the susceptibility $\chi(z)$ is directly connected to the linear absorption coefficient $\mu(z)$ [subscript q in (11) indicates that in some cases we are interested in the absorption by a definite kind of atom],

$$\mu = (2\pi/\lambda)\,\mathrm{Im}(\chi). \tag{12}$$

For the case of a uniform mirror (semi-infinite medium) we can connect the number of created photoelectrons to the loss of the radiation intensity in a differential layer, as was done in the early papers (Henke, 1972; Solomin & Kruglov, 1984). For the reflection from a semi-infinite medium we have $I(z) \propto |E(z)|^2 \mathrm{Re}(\eta)$ and $E(z) = E_0 \exp(-i\eta kz)$ ($k = 2\pi/\lambda = \omega/c$), where η is determined by (5). So

$$\mathrm{d}I/\mathrm{d}z \;\propto\; -2\,\mathrm{Re}(\eta)\,\mathrm{Im}(\eta)\,k \exp[-2\,\mathrm{Im}(\eta)\,kz]|E(0)|^2, \tag{13}$$

but for η determined by (5) we have the exact relation

$$2\,\mathrm{Re}(\eta)\,\mathrm{Im}(\eta) = \mathrm{Im}(\chi) \tag{14}$$

and we come to (11). If we are far from the total reflection region,

$$\mathrm{Im}(\eta) \simeq \mathrm{Im}(\chi)/(2\,\sin\theta), \qquad \mathrm{Re}(\eta) \simeq \sin\theta, \tag{15}$$

$$\begin{aligned} I(z) &= \left|E(0)\right|^2 \sin\theta \exp(-\mu z/\sin\theta), \\ \mathrm{d}I/\mathrm{d}z &= -\mu\left|E(0)\right|^2 \exp(-\mu z/\sin\theta), \end{aligned} \tag{16}$$

and we again come to (11). Note that the additional factor $1/\sin\theta$ in expression (1) for dn appears when the full spot of radiation intensity on the surface becomes smaller with increasing angle. Expression (11) refers to the unit surface.

The most essential difference between a multilayer sample and a semi-infinite medium is the non-exponential z-dependence of the total radiation field amplitude $\mathbf{E}(z, \omega, \theta)$. For its calculation we use the propagation matrices which describe the evolution of the tangential components of the electrical and magnetic field of radiation with z. We consider the plane waves of radiation $\sim\exp[i(\omega/c)\boldsymbol{\kappa}\mathbf{r} - i\omega t]$ and, if the dielectric tensor in a multilayer changes just along the normal to the surface $\hat{\varepsilon} = \hat{\varepsilon}(z)$, we can write

$$\boldsymbol{\kappa} = \mathbf{b} + \eta\mathbf{q}, \tag{17}$$

where $\mathbf{q}$ is the unit vector along z and $\mathbf{b}$ is a tangential component of the wavevector (in units of ω/c). In the following we shall omit the dependence of the $\hat{\varepsilon}$ and field amplitude from ω (or λ) and θ for brevity. The homogeneity of the radiation field along the surface specifies the equality of the tangential components of the wavevectors for all reflected and transmitted waves in a multilayer, *i.e.* $\mathbf{b}$ = constant, $|\mathbf{b}| = \cos\theta$ for all sublayers in a multilayer. So we shall consider the radiation field amplitudes in the form

$$\begin{bmatrix}\mathbf{E}(\mathbf{r}, t)\\ \mathbf{H}(\mathbf{r}, t)\end{bmatrix} = \begin{bmatrix}\mathbf{E}(z)\\ \mathbf{H}(z)\end{bmatrix}\exp\{i[(\omega/c)\mathbf{br} - \omega t]\}. \tag{18}$$

Then the Maxwell equations for $\mathbf{E}(z)$, $\mathbf{H}(z)$ can be written in the following way,

$$\left(\mathbf{q}^{\times}\frac{\mathrm{d}}{\mathrm{d}z} + i\frac{\omega}{c}\mathbf{b}^{\times}\right)\begin{bmatrix}\mathbf{H}(z)\\ \mathbf{E}(z)\end{bmatrix} = i\frac{\omega}{c}\begin{bmatrix}-\hat{\varepsilon}(z)\,\mathbf{E}(z)\\ \mathbf{H}(z)\end{bmatrix}, \tag{19}$$

where the superscript $\times$ symbol means the dual tensor (*i.e.* $\mathbf{q}^{\times}\mathbf{a} = \mathbf{q}\times\mathbf{a}$, $\times$ means the vector product). The system of equations (18) connects six components of the vectors $\mathbf{E}(z)$, $\mathbf{H}(z)$, but just four components are independent, because from (19) we can obtain two algebraic relations between their amplitudes,

$$(\mathbf{aH}) = (\mathbf{q}\,\hat{\varepsilon}\,\mathbf{E}), \qquad (\mathbf{aE}) = -(\mathbf{qH}), \tag{20}$$

where $\mathbf{a} = \mathbf{b}^{\times}\mathbf{q} = \mathbf{b}\times\mathbf{q}$. The tangential components of the vectors $\mathbf{E}(z)$, $\mathbf{H}(z)$,

$$\begin{pmatrix}\hat{I}\,\mathbf{H}\\ \mathbf{q}\times\mathbf{E}\end{pmatrix} = \begin{pmatrix}H_x\\ H_y\\ -E_y\\ E_x\end{pmatrix}, \tag{21}$$

should be continuous at the boundary crossing, and they are usually chosen for the task. In (21) we have used the projective operator on the surface plane $\hat{I} = -(\mathbf{q}^{\times})^2$. The coordinate system used is presented in Fig. 1.

The full vectors $\mathbf{E}$, $\mathbf{H}$ can be expressed from the tangential components (Borzdov *et al.*, 1976),

$$\begin{pmatrix}\mathbf{H}\\ \mathbf{E}\end{pmatrix} = \begin{bmatrix}\hat{I} & -\mathbf{q}\circ\mathbf{a}\\ (1/\varepsilon_q)\,\mathbf{q}\circ\mathbf{a} & \hat{I} - (1/\varepsilon_q)\,\mathbf{q}\circ\mathbf{q}\,\hat{\varepsilon}\hat{I}\end{bmatrix}\begin{pmatrix}\mathbf{H}_t\\ \mathbf{E}_t\end{pmatrix}, \tag{22}$$

where the sign $\circ$ between vectors means the outer product (the diad), $\varepsilon_q = \mathbf{q}\,\hat{\varepsilon}\,\mathbf{q}$. Finally we have

$$\frac{\mathrm{d}}{\mathrm{d}z}\begin{bmatrix}\hat{I}\,\mathbf{H}(z)\\ \mathbf{q}\times\mathbf{E}(z)\end{bmatrix} = i\frac{\omega}{c}\hat{\mathbf{M}}(z)\begin{bmatrix}\hat{I}\,\mathbf{H}(z)\\ \mathbf{q}\times\mathbf{E}(z)\end{bmatrix}, \tag{23}$$

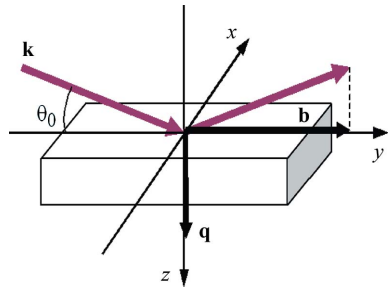

Figure 1
The coordinate system used.

where $\hat{\mathbf{M}}$ is a differential propagation matrix, the explicit expression for which is given by, for example, Borzdov *et al.* (1976),

$$\hat{\mathbf{M}} = \begin{pmatrix}\frac{1}{\varepsilon_q}\mathbf{q}^{\times}\hat{\varepsilon}\,\mathbf{q}\circ\mathbf{a} & \frac{1}{\varepsilon_q}\hat{I}\hat{\varepsilon}\hat{I} - \mathbf{b}\circ\mathbf{b}\\ \hat{I} - \frac{1}{\varepsilon_q}\mathbf{a}\circ\mathbf{a} & -\frac{1}{\varepsilon_q}\mathbf{a}\cdot\mathbf{q}\,\hat{\varepsilon}\,\mathbf{q}^{\times}\end{pmatrix}, \tag{24}$$

or, in the coordinate system used (Azzam & Bashara, 1977),

$$\hat{\mathbf{M}} = \begin{pmatrix}-\frac{\varepsilon_{yz}}{\varepsilon_{zz}}\cos\theta & 0 & \frac{1}{\varepsilon_{zz}}(\varepsilon_{yy}\varepsilon_{zz} - \varepsilon_{zy}\varepsilon_{yz}) & \frac{1}{\varepsilon_{zz}}(\varepsilon_{yz}\varepsilon_{zx} - \varepsilon_{yx}\varepsilon_{zz})\\ \frac{\varepsilon_{xz}}{\varepsilon_{zz}}\cos\theta & 0 & \frac{1}{\varepsilon_{zz}}(\varepsilon_{zy}\varepsilon_{xz} - \varepsilon_{xy}\varepsilon_{zz}) & \frac{1}{\varepsilon_{zz}}(\varepsilon_{xx}\varepsilon_{zz} - \varepsilon_{zx}\varepsilon_{xz}) - \cos^2\theta\\ 1 - \frac{\cos^2\theta}{\varepsilon_{zz}} & 0 & -\frac{\varepsilon_{zy}}{\varepsilon_{zz}}\cos\theta & \frac{\varepsilon_{zx}}{\varepsilon_{zz}}\cos\theta\\ 0 & 1 & 0 & 0\end{pmatrix}. \tag{24'}$$

Calculation of the total radiation field amplitude $\mathbf{E}(z)$ with the help of the propagation matrices is performed in two steps. Firstly the integration of (23) over the whole multilayer establishes the relation between four tangential field components on the top surface and at the substrate. This relation allows us to determine the reflected wave for a given incident wave and to obtain four tangential components of the total field (for incident plus reflected waves) on the top surface. In the second step we follow the evaluation of the tangential components of these vectors with depth by sequentially applying the propagation matrices specific for each sublayer. At each depth z we can restore the total field amplitude $\mathbf{E}(z)$ with help of (22) and use it for calculation of $A(z, \omega, \theta)$ by (10). The whole algorithm is realized in the program package *XFRAM* (Odintsova & Andreeva, 2012) and examples of fluorescence calculations from an antiferromagnetic multilayer $[\mathrm{Fe/Cr}]_n$ at the $L_{2,3}$-edge of Fe have been published by Andreeva & Odintsova (2012).

Let us consider the calculation of $\mathbf{E}(z)$ for a simpler isotropic case applicable for our experimental data. When $\hat{\varepsilon} = \hat{\varepsilon}(z)$ is a scalar function (or if this tensor is represented by a diagonal matrix in the used x, y, z basis), the σ- and π-polarized waves are independent. For σ-polarization of radiation (the electric field vector $\mathbf{E}$ for all waves is perpendicular to the reflection plane) we obtain the differential 2×2-propagation

matrix which describes the evolution with z of the $E_x = E$ and H_y components,

$$\frac{\mathrm{d}}{\mathrm{d}z}\begin{bmatrix} E_x(z) \\ H_y(z) \end{bmatrix} = i\,\frac{\omega}{c}\begin{bmatrix} 0 & 1 \\ \sin^2\theta + \chi_{xx}(z) & 0 \end{bmatrix}\begin{bmatrix} E_x(z) \\ H_y(z) \end{bmatrix}. \quad (25)$$

In (25) we insert the designation of $\chi_{xx}(z) = \varepsilon_{xx}(z) - 1$. Note that, instead of the simple exponential attenuation of the amplitude of the radiation field, at the reflection conditions we need two variables in each layer and a 2×2 propagation matrix in order to take into account the existence of two waves in each sublayer. Here they are *not* the amplitudes of the waves in the direct and opposite directions but the total amplitude of the electric field (which is actually the coherent sum of the these waves) $E = E_x$ and H_y. Often in the hard X-ray region the full electric field and its z-derivation is used, which is proportional to H_y at grazing angles.

For π-polarized radiation (the electric field vector **E** for waves in the direct and backward directions lies in the reflection plane) we obtain the differential 2×2-propagation matrix which describes the evolution of the $H_x = H$ and $-E_y$ components,

$$\hat{\mathbf{M}} = \begin{pmatrix} 0 & \varepsilon_{yy} \\ \frac{\sin^2\theta + \chi_{zz}}{\varepsilon_{zz}} & 0 \end{pmatrix}. \quad (26)$$

In the thin nth sublayer we can put $\varepsilon_{jj}(z)$ = constant and the differential equation (25) will have the analytical solution

$$\begin{bmatrix} E_x(z + d_n) \\ H_y(z + d_n) \end{bmatrix} = \exp[i(\omega/c)\hat{\mathbf{M}}_n\, d_n]\begin{bmatrix} E_x(z) \\ H_y(z) \end{bmatrix}, \quad (27)$$

where the matrix exponential $\exp[i(\omega/c)\hat{\mathbf{M}}d]$ for σ-polarization is given by the expression

$$\exp[i(\omega/c)\hat{\mathbf{M}}d] = \begin{pmatrix} \cos Q & \frac{i}{\eta}\sin Q \\ i\,\eta\,\sin Q & \cos Q \end{pmatrix}, \quad (28)$$

and $Q = (\omega/c)d_n\eta$, $\eta = (\sin^2\theta + \chi_{xx,n})^{1/2}$.

For π-polarized radiation we have

$$\exp[i(\omega/c)\hat{\mathbf{M}}d] = \begin{pmatrix} \cos Q & \frac{i\,\varepsilon_{yy,n}}{\eta}\sin Q \\ \frac{i\,\eta\,\sin Q}{\varepsilon_{yy,n}} & \cos Q \end{pmatrix}, \quad (29)$$

where $\eta = (\varepsilon_{yy,n}/\varepsilon_{zz,n})^{1/2}(\sin^2\theta + \chi_{zz,n})^{1/2}$.

A multilayer characterized by a varying susceptibility $\chi = \chi(z)$ is usually divided into thin sublayers; in each of them we can put $\varepsilon_{jj,n}(z) = 1 + \chi_{jj,n}$ = constant. The total integral propagation matrix $\hat{\mathbf{L}}(D)$ is calculated as a product of the matrix exponentials,

$$\hat{\mathbf{L}}(D) = \exp\left(i\frac{\omega}{c}d_N\hat{\mathbf{M}}_N\right)\exp\left(i\frac{\omega}{c}d_{N-1}\hat{\mathbf{M}}_{N-1}\right)\ldots\exp\left(i\frac{\omega}{c}d_1\hat{\mathbf{M}}_1\right),$$
$$D = d_1 + d_2 + \ldots + d_N. \quad (30)$$

(Layers are numerated from a surface to a substrate having the number $N + 1$.) This matrix

$$\hat{\mathbf{L}}(D) = \begin{pmatrix} L_{11} & L_{12} \\ L_{21} & L_{22} \end{pmatrix}$$

allows us to find easily the reflected wave,

$$E_\mathrm{R} = \frac{\eta_d(\eta_0 L_{12} + L_{11}) - (\eta_0 L_{22} + L_{21})}{\eta_d(\eta_0 L_{12} - L_{11}) - (\eta_0 L_{22} - L_{21})}\,E_0, \quad (31)$$

where $\eta_0 = \sin\theta$ (in the external medium we put $\varepsilon = 1$), $\eta_d = (\sin^2\theta + \chi_d)^{1/2}$, χ_d is the susceptibility of a substrate.

For the case of the σ-polarized radiation the total radiation field at the surface is

$$E(0) = E_x(0) = E_0 + E_\mathrm{R},$$
$$H_y(0) = \sin\theta\,(E_0 - E_\mathrm{R}), \quad (32)$$

and we can obtain the total radiation field amplitude $E(z)$ at any depth z (being at each depth a coherent sum of the waves in the direct and opposite directions) by successive application of the propagation matrix (28) specific at each depth to the vector column

$$\begin{bmatrix} E(z) \\ H_y(z) \end{bmatrix}$$

[or (29) to

$$\begin{bmatrix} H(z) \\ -E_y(z) \end{bmatrix}$$

in the case of the π-polarized radiation].

For calculation of the function of the electron yield $T(z)$ we use the simplest exponential attenuation function along its way, $\exp(-\varepsilon_\mathrm{e} l)$, $\varepsilon_\mathrm{e} = 1/\lambda^\mathrm{el}$, but suppose that the electron escape depth λ^el in each layer can be different and the path length l depends on the angle of emission. Using the approach of Kasrai *et al.* (1996) for the integrated electron yield over different angles of emission we describe $T(z)$ from the nth layer in the following way,

$$T_n(z) = C_1 C_2 \ldots C_{n-1}\int_0^{2\pi}\mathrm{d}\varphi\int_0^{\pi/2}\exp(-Z/\cos\psi)\sin\psi\,\mathrm{d}\psi, \quad (33)$$

where

$$Z = \left(\frac{d_1}{\lambda_1^\mathrm{el}} + \frac{d_2}{\lambda_2^\mathrm{el}} + \ldots + \frac{d_{n-1}}{\lambda_{n-1}^\mathrm{el}} + \frac{\xi_n}{\lambda_n^\mathrm{el}}\right),$$

$z = d_1 + d_2 + \ldots + d_{n-1} + \xi_n$, ξ_n is the z coordinate for the considered nth layer calculated from its top; λ_n^el is the electron escape depth in the nth layer; ψ and φ are the polar and azimuth angles of the electron yield. The integral over ψ in (32) depends on the special function $S(Z)$ called the 'exponential integral',

$$T_n(z) = 2\pi[\exp(-Z) - Z\,S(Z)],$$
$$S(Z) = \int_1^\infty \frac{\exp(-Zt)}{t}\,\mathrm{d}t. \quad (34)$$

In our program we calculate $S(Z)$ numerically.

According to Ejima (2003) we include in (33) the additional factors C_i describing the transmission probability through the interface between the $(i-1)$th and ith layers originating from the difference in the electric potential in these layers. In the computing procedure we combine constant factors $C_1C_2\ldots C_{n-1}$ and the probability of the electron creation τ_n into one single factor for each nth layer.

Note that the exponential attenuation in (33) for the description of the electron propagation is not exactly correct, because the electrons change the direction of their propagation owing to the collisions with other electrons beside creating secondary electrons. The Monte Carlo method gives the most adequate picture of the electron propagation in the medium (see, for example, Liljequist *et al.*, 1978; Kovalchuk *et al.*, 1986; Bakaleinikov *et al.*, 2001; Jablonski & Powell, 2002). However, in our case of very soft radiation the sampling depth of the electrons is so small that the exact function for the electron yield $T(z)$ does not have much influence on the final result.

3. Experimental data

The experimental data have been obtained for a SiO_2/Si/SiO_2/c-Si sample at different glancing angles for σ-polarized soft X-rays which demonstrated the strong influence of the reflectivity on TEY spectra. The samples have a specific structure called 'silicon-on-insulator' (Fig. 2). A ~150 nm silicon oxide SiO_2 layer and then a strained silicon nanolayer, ~100 nm thick, were deposited on a single-crystalline Si (100) substrate, about 300 μm thick. It is clear that the surface of the sample has been oxidized in the air and typically the thickness of the top native oxide layer is ~2 nm. So in total we have the structure SiO_2/Si/SiO_2/c-Si. However, the reflectivity of the soft X-rays was actually determined by the three top layers SiO_2(2 nm)/Si(10–100 nm)/SiO_2, having SiO_2 as substrate. In this paper we consider the results for one sample with a strained Si layer of thickness ~80 nm and characterized by the yellow colour of its surface.

XANES spectra near the $L_{2,3}$ absorption edges of Si for this sample have been measured for different glancing angles at the SRC (Synchrotron Radiation Center, University of Wisconsin-Madison, Stoughton, USA) and BESSY II (Helmholtz Zentrum, Berlin, Germany) synchrotron radiation facilities. The sample current technique was used. Details of the experiment have been presented by Domashevskaya *et al.* (2011).

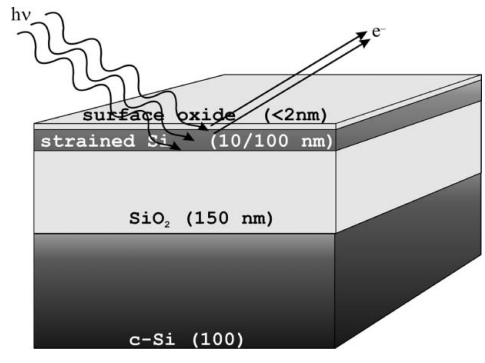

Figure 2
Schematic view of the sample.

The experimental results are shown in Fig. 3 (left side). The normal-incidence spectrum is shown at the top of the figure. It is typical of the oxidized Si sample (Domashevskaya *et al.*, 2011). The XANES spectrum of the standard sample (s-Si) consists of two basic absorption edges, the Si $L_{2,3}$-edges of elementary Si (100 eV) and the Si $L_{2,3}$-edges of natural oxide (105.5 eV). The fine doublet structure of the basic edges is caused by the spin-orbital splitting of the $2p_{1/2,3/2}$ Si core level (0.6 eV) from which electrons transfer to the Si and SiO_2 conduction band under synchrotron beam excitation. The fine structure of the Si $L_{2,3}$ basic edges (~100 eV and ~103 eV) is characteristic of single-crystalline silicon independent of its conduction type and orientation [(100) or (111)] and disappears into amorphous silicon a-Si for which only one step (~100.5 eV) remains. However, investigation of the XANES fine structure of pure Si for sample characterization is almost impossible owing to the existence of the SiO_2 top layer and the small sampling depth of the TEY method. It is not revealed in our normal-incidence spectrum. This is why we have attempted to obtain further information by changing the angle of incidence. The underlying layer of crystalline Si is revealed in XANES spectra measured at small glancing angles of incident radiation in a quite unexpected manner.

At small glancing angles (5, 7, 9, 11, 13, 15, 17, 19, 21, 25°) the measured TEY spectra dramatically differ from the normal-incidence spectrum. They exhibit oscillations at the per-edge energy range 90–100 eV. Surprisingly the phase of

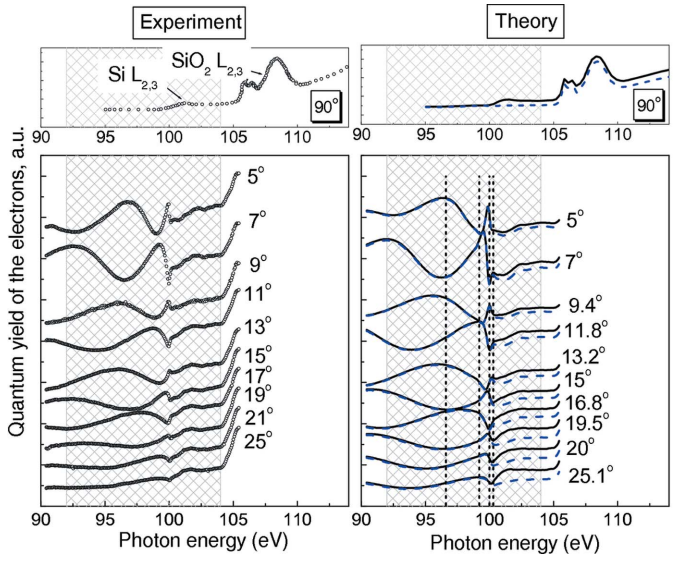

Figure 3
TEY spectra for the normal incidence of radiation (top panels) and at glancing angles of 5, 7, 9, 11, 13, 15, 17, 19, 21, 25° (below, vertically shifted). Experimental spectra are on the left-hand side and the results of our fit are on the right-hand side. Dashed lines (blue) on the right-hand side present the electron yield from the top oxidized layer only, ~2.2 nm thick. The shaded area denotes the energy range for the fit of the glancing incidence spectra. Dotted vertical lines mark the energies for which the angular dependencies are calculated (see also Fig. 7).

the oscillations switches sign if the glancing angle is changed by $\sim 2^\circ$. Besides, an abrupt jump (a rostrulum up or a rostrulum down) of the intensity is observed near 100 eV (Si L_3-edge). In the hard X-ray region, decreasing the glancing angle is commonly used in order to decrease the investigated depth of the sample. In our experiment the sampling depth is extremely small even at the normal incidence of radiation ($\sim$1–2 nm). In the normal-incidence XANES spectrum mostly SiO_2 $L_{2,3}$ peaks dominate, whereas pure Si $L_{2,3}$ peaks have very low intensity. The specific features of the experimental TEY spectra at glancing angles do not occur in the normal-incidence spectra, so they are not the properties of the top layer of material itself but appear owing to the interaction of the incident radiation with the whole multilayer structure.

4. Interpretation of the data

The fit of the data was not simple because the reflectivity had not been measured either on the energy scale or on the angular scale. Information about the optical constants for Si and SiO_2 in the vicinity of the $L_{2,3}$-edges is quite unreliable in standard tables and in the literature.

Some data from different sources for the real and imaginary parts of the susceptibilities of Si and SiO_2 for the energy range under investigation are presented in Fig. 4. We see that the data are rather different. Therefore, during the fit procedure the optical constants for the Si, SiO_2-'substrate' and oxidized 'cap' SiO_2-layer were varied. We tried to keep the overall shape of the susceptibility energy dependencies (and control the agreement of our calculations for $\theta = 90^\circ$ with the normal-incidence spectrum), but used the additional variable factors (12 fit parameters) for the shift and multiplication for each curve. We partially used a manual fit of the parameters, but an automatic fit was also applied (like the *AMOEBA* code, sequent one-parameter descent and multi-dimensional NET calculations). We also changed the inclination of the low-energy 'tail' of the susceptibility dependencies in the energy region 90–98 eV for pure Si in the middle layer and in the 90−103 eV region for SiO_2 in the top and third layers (additional six fit parameters) where the most interesting features appear on the experimental Y spectra. The resulting susceptibility dependencies for three layers are shown in Fig. 4 by the thick lines.

The susceptibility of the bottom SiO_2 layer does not influence the resulting TEY spectra heavily, so we have kept the dependencies presented by Filatova *et al.* (1999) but were forced to slightly shift the absolute value of the real part. For the middle Si layer we started from the data of Henke (1993), but a small energy shift is needed for a better correspondence of the experimental and theoretical normal-incidence Y spectrum. We have found as well that the absolute value of the imaginary part of χ in pure Si should be magnified [this is partly correlated with the data from NIST (Chantler *et al.*, 2009)]. The shape of the real part of χ in the Si layer in the pre-edge region (marked by the circle in Fig. 4) has been changed in order to obtain the appearance of the 'rostrulum up' or 'rostrulum down' features in the TEY dependencies at glancing angles.

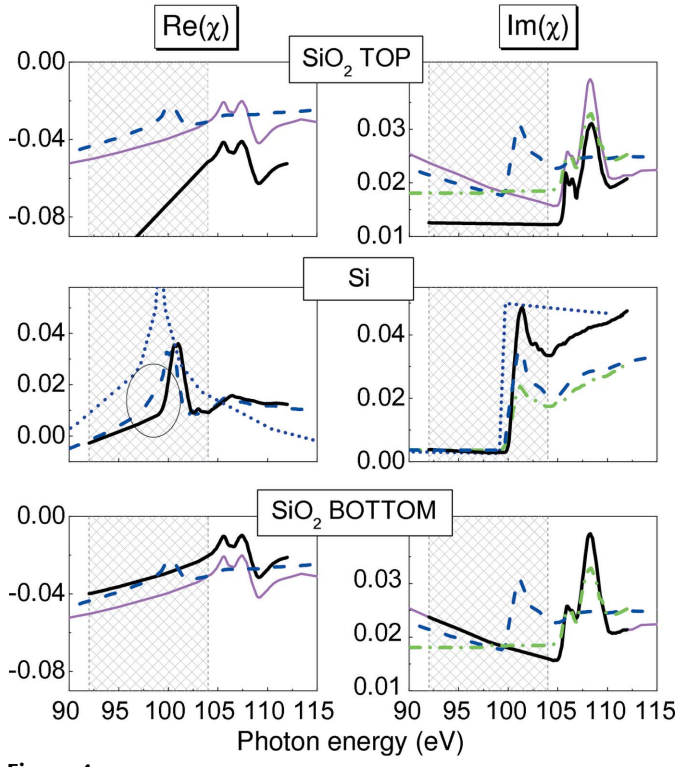

Figure 4
Real and imaginary parts of the Si and SiO_2 susceptibility in the vicinity of the $L_{2,3}$ absorption edges of Si for three layers in our structure. Dashed lines (blue) for Si and SiO_2 present data from the tables of Henke *et al.* (1993); thin solid lines (magenta) for SiO_2 are the results from Filatova *et al.* (1999); dash-dotted lines (green) are the absorption data from Kasrai *et al.* (1996), normalized to the absolute values of Henke *et al.* (1993) 'at the tails'; dotted lines (dark blue) for Si are data from NIST (Chantler *et al.*, 2009); bold lines (black) are data obtained by the fit of the experimental data for three layers in our structure. The shaded area denotes the energy range for the fit of the glancing incidence spectra.

The energy dependencies of susceptibilities in the top oxidized layer were essentially modified during the fit procedure. The essential change of the optical constants in the top layer was expected owing to the imperfections in the ultrathin layer structure (induced distortion of the elementary cell, defects, dislocations, impurities, *etc.*). Typically for hard X-rays the electronic density becomes lower (by $\sim$10–20%) in the top layer, but in our case we have found the opposite result: the absolute value of the real part of the susceptibility was found to be larger than the tabled values for SiO_2. The relation between the electronic density and the optical constants is more complicated in the soft X-ray region, *e.g.* oxidation leads to an increase in the absolute values of the real and imaginary parts of χ. The result obtained for the top layer can be explained by the reason that the top 2.2 nm-thick oxidized layer can contain some impurities, *e.g.* absorbed atoms C, N, *etc.* To be sure that these impurities can influence the optical constants in this way we have taken the tabled data from *XOP* (http://www.esrf.eu/UsersAndScience/Experiments/TBS/SciSoft/xop2.3/Main) for Re(χ) and Im(χ) for different compounds of silicon (Fig. 5). It can be clearly seen that

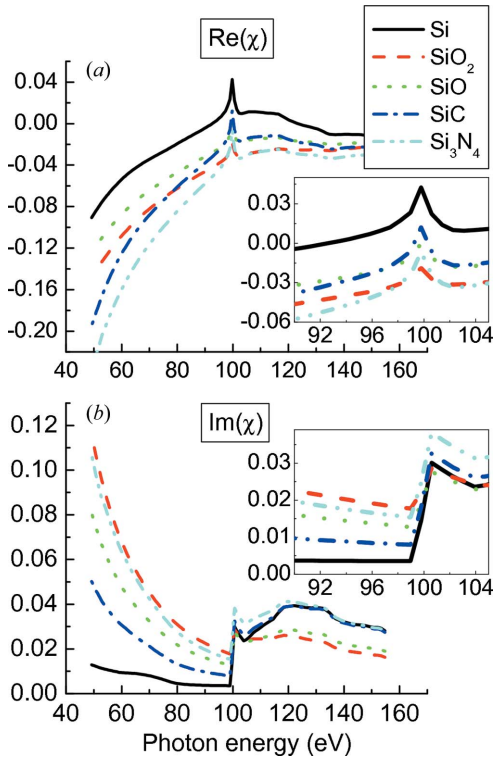

Figure 5
Table dependencies from ESRF software *XOP* of the optical constants for different compounds of Si. In the inserts these dependencies are drawn in the energy range considered in our fit.

compounds like SiC or Si_3N_4 are characterized by an increase in the absolute values of Re(χ) and a decrease in Im(χ) in the pre-edge region compared with the optical parameters of SiO_2. By our fit we have obtained exactly such a tendency for the top SiO_2 layer.

More accurate determination of the optical constants for the layers can be obtained by measurements of the angular dependencies of the reflectivity and TEY for different energies, as was carried out by, for example, Gupta *et al.* (2007) and Smekhova *et al.* (2010). Unfortunately we had no such experimental data; for soft X-rays such data can only be obtained at specialized synchrotron radiation beamlines.

The thickness $d_{1,2}$ of the top SiO_2 layer and strained Si layer were varied as well as the electron escape depth λ_n^{el} (additional four fit parameters). For λ_n^{el} we obtain the values 1.47 nm for SiO_2 (n = 1) and 0.81 nm for Si (n = 2), close to those used by Kasrai *et al.* (1996). The fit also gives the thickness of the top oxide layer d_{SiO2} = 2.2 nm and the thickness of the strained Si layer d_{Si} = 85.8 nm. Finally, a reasonable agreement between the theoretical and experimental energy dependencies for all angles of incidence including 90° (Fig. 3, compare left- and right-hand parts) has been achieved. We have reproduced the oscillations in the pre-edge region of the Si L-edge, changing the phase with the angle variation, and have obtained rostrulum-up and rostrulum-down features at the Si absorption edge.

As long as our calculations are based on the exact solutions of the electromagnetic theory for a radiation field inside a multilayer, it is possible to explain the reasons for the intriguing energy dependencies of the TEY spectra at small glancing angles of radiation.

Initially we suppose that the peculiarities of the Y spectra at different angles are explained by the enhancement of the field in the middle Si layer because the main anomalous features were observed near the $L_{2,3}$-edges of pure Si but not at the top SiO_2. However, the very small escape depth for our low-energy electrons ($\lambda_{el} \propto 1$ nm) contradicts this assumption. In Fig. 3, on the right-hand side, we also present the contribution from the top SiO_2 layer (dashed blue lines) in addition to the quantum yield Y and we see that the main features of the Y spectra in the pre-edge region are completely determined by this contribution. So the role of the underlying Si layer is different. The strong variation of the Si optical constants near the $L_{2,3}$-edges dramatically changes the total radiation field $|E(z, \omega, \theta)|^2$ in the top SiO_2 layer from which we actually measure the quantum yield Y. This explanation is illustrated in Fig. 6. The presented depth dependencies of $|E(z)|^2$ (standing waves) for the selected photon energies at two grazing angles of the incident radiation clearly show that the wisp or lapse on the TEY spectrum is caused by the specific waveguide modes in the middle Si layer. If on the top boundary of the Si layer we have the node of the standing wave, the measured TEY intensity decreases; if we have the anti-node then the TEY intensity from the top layer increases. This observed effect in the energy scale is similar to the calculated angular dependency of TEY from a thin layer in an earlier paper (Pepper, 1970).

The abrupt change of the TEY intensity near 100 eV is explained by the substantial suppression of the waveguide mode in the Si layer by a huge increase in the absorption in this layer exactly at the Si absorption edge. The wave reflected from the bottom boundary of the Si layer becomes negligible, the enhancement of the intensity by the interference of the waves in direct and opposite directions disappears, and the next oscillation on the TEY spectrum drops off.

The suppression of the reflectivity from the bottom boundary of the Si layer and its influence on the TEY electron yield is also illustrated by the angular dependencies presented in Fig. 7. We see that the small change of the photon energy from 100 eV to 100.3 eV leads to the suppression of the oscillatory dependences of the reflectivity and TEY.

In Fig. 7 we compare the $(1 - R)$ and $|E(0)|^2$ angular dependencies. They are not identical because in the case of a multilayer the reflectivity is not described by the simple Fresnel formula and relation (3) does not take place. The TEY dependency is rather close to the $|E(0)|^2$ angular dependency (because the main contribution to our Y spectra is from the very surface), but not to $(1 - R)$. This is an illustration of the non-applicability of formula (1) for the case of multilayers.

However, the energy dependencies of Y, $(1 - R)[\mathrm{Im}(\chi_1)]/\lambda$ and $|E(0)|^2[\mathrm{Im}(\chi_1)]/\lambda$ are quite different (Fig. 8), so we should conclude that the contribution from the second pure Si layer noticeably influences the TEY energy dependences mainly due to the factor $\mu_{Si}(\lambda) \propto \mathrm{Im}[\chi_{Si}(\lambda)]/\lambda$.

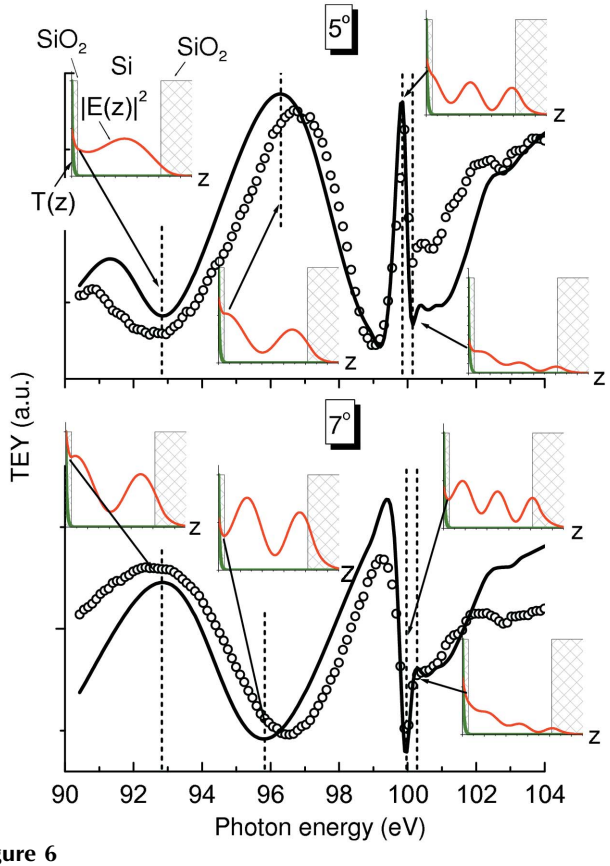

Figure 6
Experimental (symbols) and theoretical (solid lines) energy dependencies of TEY spectra for the glancing angles 5° and 7°. In the inserts we show the depth dependencies of $|E(z)|^2$ (standing waves) for the photon energies, indicated by the vertical dashed lines. Function $T(z)$ (green) presented in the inserts is almost unseen because it is concentrated in the top SiO_2 layer.

5. Conclusions

We have shown that the remarkable features of the quantum yield spectra measured in the vicinity of the Si $L_{2,3}$ absorption edges at different glancing angles are not caused by some specific changes of the XANES spectra but originate from optical phenomena. TEY spectra are influenced by the reflectivity formed by the whole multilayer structure. The special structure of the investigated SiO_2/Si/SiO_2 multilayer has allowed us to enhance and reveal such influence in the most impressive way owing to the formation of the waveguide modes in the middle Si layer. In principle, such a change of the TEY spectra by the angle variation can be used as an additional source of information for determination of the absolute value of the optical constants because the precise matching of the optical parameters in the structure is required for the appearance of the waveguide effect. However, the task of determining the optical constants could be better solved if complimentary measurements of the reflectivity are performed.

This work is based in part upon research performed at the Synchrotron Radiation Center, University of Wisconsin-Madison, which is supported by the National Science Foundation under award No. DMR-0537588. Authors are grateful for support of this work to the Director, official BESSY administration, BESSY Beamtime Allocation Committee and Coordinators of Russian–German Beamline facility. This work is based upon research supported by the Federal Targeted Program 'Scientific and Scientific Educational Personnel of the Innovative Russia'. The work was also supported by RFBR grants 09-02-01293-a, 10-02-00768-a, 12-02-00924-a.

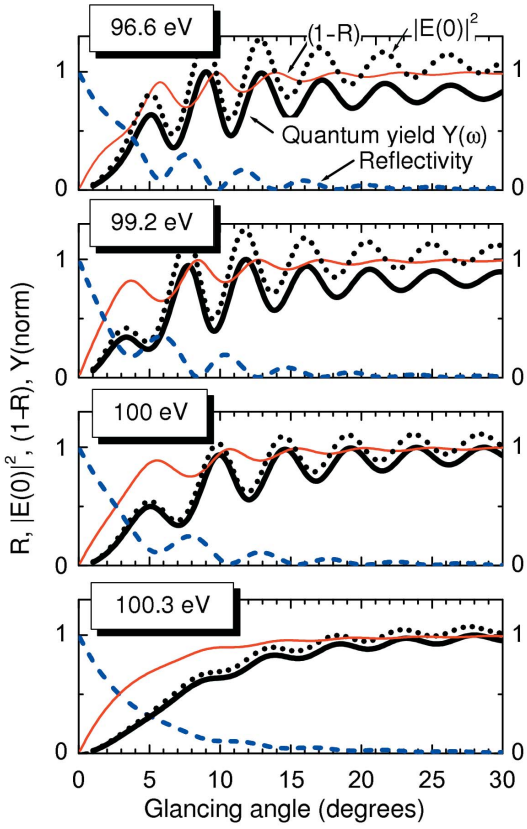

Figure 7
Angular dependencies of the reflectivity R (dashed blue lines), the square module of the field on the surface $|E(0)|^2$ (dotted black lines), $(1 - R)$ dependencies (thin red lines) and calculated TEY angular dependencies (thick black lines) for different energies in the vicinity of the Si $L_{2,3}$ absorption edges indicated in Fig. 3 by dashed vertical lines.

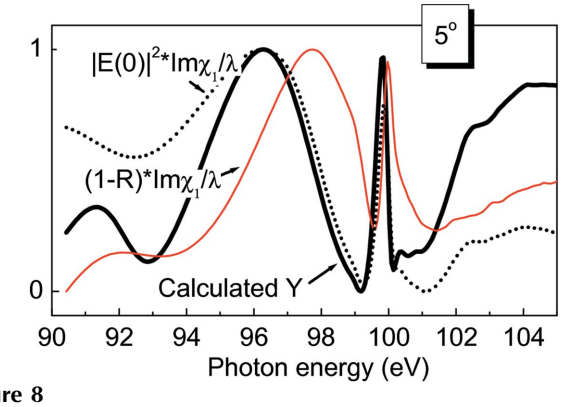

Figure 8
The energy dependencies of the quantum yield Y, calculated by the exact theory (6), (11) for the structure model, obtained by our fit (thick solid line), $(1 - R)\,\mathrm{Im}(\chi_1)/\lambda$ (thin red solid line) and $|E(0)|^2\,\mathrm{Im}(\chi_1)/\lambda$ (dotted black line) for a 5° glancing angle. All curves are normalized.

References

Afanas'ev, A. M. & Kohn, V. G. (1978). *Zh. Eksp. Teor. Fiz.* **74**, 300–313. (*Sov. Phys. JETP*, **47**, 154–156.)

Andrė, J. M., Barchewitz, R., Maquet, A. & Marmoret, R. (1984). *Phys. Rev. B*, **30**, 6576–6585.

Andreeva, M. A., Belozerskii, G. N., Irkaev, S. M., Semenov, V. G., Sokolov, A. Yu. & Shumilova, N. V. (1991). *Phys. Status Solidi A*, **127**, 455–464.

Andreeva, M. A., Gribova, A. D., Odintsova, E. E., Borisov, M. M., Kovalchuk, M. V. & Mukhamedzhanov, E. Kh. (2009). *Moscow Univ. Phys. Bull.* **64**, 437–441.

Andreeva, M. A., Irkaev, S. M. & Semenov, V. G. (1994). *JETP*, **78**, 956–965.

Andreeva, M. A., Irkaev, S. M. & Semenov, V. G. (1996). *Hyperfine Interact.* **97/98**, 605–623.

Andreeva, M. A., Irkaev, S. M., Semenov, V. G., Prokhorov, K. A., Salashchenko, N. N., Chumakov, A. I. & Rüffer, R. (1999). *J. Alloys Compd.* **286**, 322–332.

Andreeva, M. A. & Odintsova, E. E. (2012). *Moscow Univ. Phys. Bull.* **67**, 196–200.

Andreeva, M. A., Smekhova, A. G., Lindgren, B., Björck, M. & Andersson, G. (2006). *J. Magn. Magn. Mater.* **300**, e371–e374.

Azzam, R. M. & Bashara, N. M. (1977). *Ellipsometry and Polarized Light.* Amsterdam: North Holland.

Bakaleinikov, L. A., Flegontova, E. Yu., Pogrebitskii, K. Yu., Lee, H.-J., Cho, Y.-K., Park, H.-M. & Song, Y.-W. (2001). *Tech. Phys.* **46**, 796–805.

Barchewitz, R., Cremonese-Visicato, M. & Onori, G. (1978). *J. Phys. C*, **11**, 4439–4445.

Bedzyk, M. J., Bommarito, G. M. & Schildkraut, J. S. (1989). *Phys. Rev. Lett.* **62**, 1376–1379.

Bera, S., Bhattacharjee, K., Kuri, G. & Dev, B. N. (2007). *Phys. Rev. Lett.* **98**, 196103.

Bergmann, A., Grabis, J., Nefedov, A., Westerholt, K. & Zabel, H. (2006). *J. Phys. D*, **39**, 842–850.

Boer, D. K. G. de (1991). *Phys. Rev. B*, **44**, 498–511.

Bohlen, A. von (2009). *Spectrochim. Acta B*, **64**, 821–832.

Born, M. & Wolf, E. (1968). *Principles of Optics.* Oxford: Pergamon.

Borzdov, G. N., Barkovskii, L. M. & Lavrukovich, V. I. (1976). *Zh. Prikl. Spectrosk.* **25**, 526–531.

Bremer, J., Kaihola, K. & Keski-Kuha, R. (1980). *J. Phys. C*, **13**, 2225–2230.

Brug, H. van, van Dorssen, H. & van der Wiel, M. J. (1989). *Surf. Sci.* **210**, 69–84.

Chantler, C. T., Olsen, K., Dragoset, R. A., Chang, J., Kishore, A. R., Kotochigova, S. A. & Zucker, D. S. (last updated 2009). *Database of the National Institute of Standards and Technology (NIST)*, http://physics.nist.gov/PhysRefData/FFast/html/form.html.

Dev, B. N., Das, A. K., Dev, S., Schubert, D. W., Stamm, M. & Materlik, G. (2000). *Phys. Rev. B*, **61**, 8462–8468.

Domashevskaya, E. P., Terekhov, V. A. & Turishchev, S. Yu. (2011). *J. Surf. Invest.* **5**, 141–149.

Ejima, T. (2003). *Jpn. J. Appl. Phys.* **42**, 6459–6466.

Ejima, T., Ouchi, K. & Watanabe, M. (1999). *J. Electron Spectrosc. Relat. Phenom.* **101–103**, 833–838.

Fedorov, F. I. (1976). *Theory of Gyrotropy.* Minsk: Nauka I Tekhnika. (In Russian.)

Filatova, E. O., Jonnard, P. & André, J.-M. (2006). *Thin Solid Films*, **500**, 219–223.

Filatova, E., Lukyanov, V., Barchewitz, R., André, J. M., Idir, M. & Stemmler, Ph. (1999). *J. Phys. Condens. Matter*, **11**, 3355–3370.

Filatova, E., Stepanov, A., Blessing, C., Friedrich, J., Barchewitz, R., Andre, J.-M., Guern, F., Le, Bac, S. & Troussel, P. (1995). *J. Phys. Condens. Matter*, **7**, 2731–2744.

Goering, E., Will, J., Geissler, J., Justen, M., Weigand, F. & Schuetz, G. (2001). *J. Alloys Compd.* **328**, 14–19.

Gudat, W. & Kunz, C. (1972). *Phys. Rev. Lett.* **29**, 169–172.

Gupta, A., Kumar, D. & Meneghini, C. (2007). *Phys. Rev. B*, **75**, 064424.

Henke, B. L. (1972). *Phys. Rev. A*, **6**, 94–104.

Henke, B. L., Gullikson, E. M. & Davis, J. C. (1993). *At. Data Nucl. Data Tables*, **54**, 181–342 (see also http://henke.lbl.gov/optical_constants/getdb2.html).

Jablonski, A. & Powell, C. J. (2002). *Surf. Sci. Rep.* **47**, 33–91.

Jones, R. G. & Woodruff, D. P. (1982). *Surf. Sci.* **114**, 38–46.

Kaihola, L. & Bremer, J. (1981). *J. Phys. C*, **14**, L43–L47.

Kao, C.-C., Chen, C. T., Johnson, E. D., Hastings, J. B., Lin, H. J., Ho, G. H., Meigs, G., Brot, J.-M., Hulbert, S. L., Idzerda, Y. U. & Vettier, C. (1994). *Phys. Rev. B*, **50**, 9599–9602.

Kasrai, M., Lennard, W. N., Brunner, R. W., Bancroft, G. M., Bardwell, J. A. & Tan, K. H. (1996). *Appl. Surf. Sci.* **99**, 303–312.

Kim, S. K. & Kortright, J. B. (2001). *Phys. Rev. Lett.* **86**, 1347–1350.

Knabben, D., Weber, N., Raab, B., Koop, Th., Hillebrecht, F. U., Kisker, E. & Guo, G. Y. (1998). *J. Magn. Magn. Mater.* **190**, 349–356.

Koval'chuk, M. V. & Kohn, V. G. (1986). *Sov. Phys. Usp.* **29**, 426–446.

Kovalchuk, M. V., Liljequist, M. V. & Kohn, V. G. (1986). *Fiz. Tverd. Tela*, **28**, 3409–3416. (*Sov. Phys. Fiz. Tverd. Tela*, **28**, 1918–1922.)

Lee, T., Joumard, I., Zegenhagen, J., Brandt, M. & Schoch, V. (2006). *ESRF Newsl.* **43**, 18.

Liljequist, D., Ekdahl, T. & Baverstam, U. (1978). *Nucl. Instrum. Methods*, **155**, 529–538.

Lyakhovskaya, I. I., Shulakov, A. C., Lobanova, L. E. & Zimkina, T. M. (1988). *Fiz. Tverd. Tela*, **30**, 221–226.

Novikova, N. N., Zheludeva, S. I., Kovalchuk, M. V., Stepina, N. D., Erko, A. I. & Yur'eva, E. A. (2009). *Crystallogr. Rep.* **54**, 1208–1213.

Odintsova, E. E. & Andreeva, M. A. (2010). *J. Surf. Invest.* **4**, 913–922.

Odintsova, E. E. & Andreeva, M. A. (2012). *XFRAM*, http://kftt.phys.msu.ru/programs/XFRAM.zip.

Oppeneer, P. M., Mertins, H.-Ch, Abramsohn, D., Gaupp, A., Gudat, W., Kunes, J. & Schneider, C. M. (2003). *Phys. Rev. B*, **67**, 052401.

Pepper, S. V. (1970). *J. Opt. Soc. Am.* **60**, 805–812.

Rumsh, M. A., Lukirskii, M. A. & Shchemelev, V. N. (1961). *Izv. Akad. Nauk SSSR Ser. Fiz.* **25**, 1060–1065.

Sacchi, M. (1999). *Rass. Sci.* **4**, 3–13.

Smekhova, A. G., Andreeva, M. A., Odintsova, E. E., Dufour, C., Dumesnil, K., Wilhelm, F. & Rogalev, A. (2010). *Crystallogr. Rep.* **55**, 854–862.

Solomin, I. K. & Kruglov, M. V. (1984). *Fiz. Tverd. Tela*, **26**, 519–523.

Terekhov, V. A., Turishchev, S. Yu., Pankov, K. N., Zanin, I. E., Domashevskaya, E. P., Tetelbaum, D. I., Mikhailov, D. I., Belov, A. I. & Nikolichev, D. E. (2011). *J. Surf. Invest.* **5**, 958–967.

Terekhov, V. A., Turishchev, S. Yu., Pankov, K. N., Zanin, I. E., Domashevskaya, E. P., Tetelbaum, D. I., Mikhailov, A. N., Belov, A. I., Nikolichev, D. E. & Zubkov, S. Yu. (2010). *Surf. Interface Anal.* **42**, 891–896.

Vartanyants, I. A. & Koval'chuk, M. V. (2001). *Rep. Prog. Phys.* **64**, 1009–1084.

Vartanyants, I. A. & Zegenhagen, J. (1997). *Il Nuovo Cimento*, D**19**, 617–624.

Waki, I. & Hirai, Y. (1989). *J. Phys. Condens. Matter*, **1**, 6755–6762.

Watanabe, M., Ejima, T., Miyafa, N., Imazono, T. & Yanagihara, M. (2006). *Nucl. Sci. Tech.* **17**, 257–267.